Geohazard Mechanics 4 (2026) 1–9

Contents lists available at ScienceDirect

Geohazard Mechanics

journal homepage: www.keaipublishing.com/en/journals/geohazard-mechanics

Fracture evolution of deep coals in true tri-axial hydraulic fracturing experiment

Xin Zhang[a], Guangyao Si[a,*], Anye Cao[b,**], Changbin Wang[b], Guozhen Zhao[a,c]

[a] School of Minerals and Energy Resources Engineering, University of New South Wales, Sydney, 2052, NSW, Australia
[b] State Key Laboratory of Coal Exploration and Intelligent Mining, China University of Mining and Technology, Xuzhou, 221116, China
[c] College of Mining Engineering, Taiyuan University of Technology, Taiyuan, 030024, China

ARTICLE INFO

Keywords:
Tri-axial hydraulic fracturing
Acoustic emission
Fracture evolution
Coal heterogeneity

ABSTRACT

Deeper exploitation of coal resources faces higher possibility of rockburst and mining earthquake. Hydraulic fracturing (HF) proved to be an effective solution in coal mines but its monitoring and evaluation remains unexplored. This study presents a true triaxial hydraulic fracturing experiment with acoustic emission (AE) recording, conducted on a 150 mm cubic coal sample from a deep underground mine. Fracture evolution was analysed based on 539 localized events using a modified simplex method. According to the injection history, AE counts and energy evolution, the coal undergoes initiation, intersection, and breakdown stages. The AE energy peak lags behind the water pressure peak due to the dilatancy effect. Rapid fluctuations in water pressure trigger peak AE event rates, often followed by silent periods with minimal AE activity, which can serve as precursors for crack prediction. The distribution of AE events indicates that fractures originate from the naked borehole and propagate upward, predominantly accumulating in the middle and upper regions of the coal sample. At low water pressure, fractures extend primarily along the maximum principal stress direction, while at high water pressure, they diffuse spherically. The uneven transition and storage of crack energy during injection lead to alternating shrinkage and expansion of AE event distribution as water pressure increases. In addition, coal heterogeneity plays a significant role in fracture formation, resulting in tortuous hydraulic fracture planes that deviate from alignment with the maximum principal stress.

1. Introduction

As mining operation extends to greater depths, it encounters higher tectonic stress. This environment elevates the risk of dynamic disasters, such as rock bursts, and coal and gas outbursts. Hydraulic fracturing (HF) has been largely used to be the precondition the rock strata in coal mines as a strategy for preventing from the dynamic disasters [1,2]. Some new theories and methods of hydraulic fracturing have been developed such as pulse HF [3], cyclic HF and repeatable HF [4]. They have been employed in coal mines successfully to measure crustal stress of surrounding rock matrix, to increase falling possibility of roof coal, and to prevent ground controlling related accidents [5]. Additionally, HF has proven beneficial in improving the permeability of rock and coal seams, reducing gas pressure, and preventing coal-methane outbursts [6–8].

Although hydraulic fracturing in coal mines has advanced significantly in terms of equipment and operation, its monitoring and evaluation remain a major challenge. Studies have shown that the microseismic (MS) and acoustic emission (AE) signals generated by coal and rock fracturing contain valuable information about fracture initiation and propagation, enabling the reconstruction of the cracking process [9–11]. This reconstruction relies on the accurate localisation of MS/AE events. Common localisation methods include the simplex method [12], grid search [13], Bayesian differential evolutionary inversion [14], double-difference method [15], and particle swarm optimization differential evolution algorithm [16]. While these techniques have been successfully applied in hydraulic fracturing for oil and gas industries, their practical use in coal mine hydraulic fracturing (CMHF) for analysing the spatial dynamics of fractures remains limited. Compared to oil and gas reservoirs, coal mines present a more complex

* Corresponding author.
** Corresponding author.
E-mail addresses: g.si@unsw.edu.au (G. Si), caoanye@163.com (A. Cao).
Peer review under the responsibility of Liaoning University.

https://doi.org/10.1016/j.ghm.2025.12.002
Received 9 March 2025; Received in revised form 20 August 2025; Accepted 30 December 2025
Available online 31 December 2025

geological environment and a highly heterogeneous signal propagation medium. Additionally, MS events induced by CMHF typically have lower energy levels, and signal quality degrades significantly over long distances, making it difficult to accurately capture and interpret fracture initiation and propagation [17]. Given the small scale and weaker amplitudes associated with CMHF, more precise signal acquisition and localisation techniques are required. A systematic and specialized investigation into hydraulic fracturing in coal mines is essential to improve monitoring accuracy and fracture characterization.

Studying in-situ coal mine hydraulic fracturing (CMHF) directly is extremely challenging, if not impossible, due to various complexities such as coal-rock seam groupings, pre-existing joints and fissures, and intricate underground constructions. Given these constraints, laboratory-scale coal sample experiments provide a more practical and reliable starting point [10,18,19]. Additionally, coal sample hydraulic fracturing has significant implications for improving CMHF at an engineering scale, as direct coal seam fracturing is commonly applied in mining faces to facilitate roof coal detachment [20,21]. Recent laboratory studies on hydraulic fracturing typically use small cubic or cylindrical samples subjected to confining and axial compressive loading. These samples are often composed of rock, cement, or simulated coal, whereas true triaxial hydraulic fracturing experiments on large coal samples remain relatively rare [22,23]. Larger coal samples better represent in-situ conditions but are inherently weaker than rocks and exhibit higher heterogeneity, leading to more complex fracture propagation behaviours. Understanding the dynamic evolution of coal fracturing under triaxial stress is essential for prevention and management of rockburst and associated damage. This study conducted true triaxial hydraulic fracturing on coal samples obtained from deep underground mines with high risk of rockburst, concluded the propagation of hydraulic fractures at different injection stages by localising acoustic emission (AE) events and computing AE energy, and analysed the heterogeneity of coal and its influence on fracture evolution and final fracture morphology.

2. Experimental equipment and test design

The coal samples used in this study were extracted from a depth of 850 m in the Xiezhuang Coal Mine in China, which is prone to high risk of rockburst. The strength of the coal was evaluated following the International Society for Rock Mechanics (ISRM) standard test procedures to provide a reference for principal stress configuration and serve as a basis for rock failure analysis. To determine the uniaxial compressive strength, coal cylinders equipped with strain gauges were subjected to loading at a rate of 0.5 MPa/s [24]. The fundamental elastic properties of the coal are summarised in Table 1. The true triaxial hydraulic fracturing experiments were conducted using a self-designed loading and monitoring system. As illustrated in Fig. 1a, the apparatus comprises three main components: the stress loading system, the water injection system, and the AE monitoring system. These systems operate independently and are controlled by separate computers.

The 150 mm cubic coal sample is drilled with an injection borehole of 20 mm diameter and 60 mm length at the centroid of top surface. A hole packer with 60 mm length is glued with the injection borehole by epoxy anchoring adhesive. To guide a reasonable initiation of hydraulic fractures, the void section of 30 mm long and 20 mm diameter is extended from the bottom of injection borehole. The configured sample is positioned at the centre of the loading frame and injected with water through an L-shaped inner pipe embedded in the upper loading disc, as shown in Fig. 1b. Twelve AE sensors are horizontally embedded within the surrounding loading discs to capture fracture-induced signals. The precise locations of all AE sensors are detailed in Table 2. What is worth noting that the natural coal formation is full of beddings and preexisting fractures [10], which makes it difficult to prepare larger intact cubic than 150 mm side length in the laboratory. Therefore, this size is suitable for investigation into the initiation and propagation of hydraulic fractures around the injection boreholes, which can dominate the far field extension of hydraulic fractures in the field operation at coal mines.

Table 1
Properties of tested coal sample.

Rock property	Value
Uniaxial compression strength (UCS) (MPa)	5.99
Tensile strength (MPa)	0.64
Young's modulus (GPa)	7.89
Density (kg/m^3)	2.6 × 10^3
Poisson's ratio	0.42
P wave velocity (m/s)	3000

As illustrated in Fig. 1b, six loading discs from three orthogonal directions advance simultaneously to establish firm contact with the sample's walls, while the hole packer on the top surface is sealed and pressurized. AE sensors are embedded within the horizontal load plates, ensuring tight adhesion to the sample for accurate signal acquisition. To calibrate all AE sensors, a lead break test is performed on the four horizontal surfaces before the experiment. During the lead break test, all the waveforms generated on each surface are required to be similar in amplitude to ensure the satisfying coupling between the AE sensors and the coal sample. Once the desired stress levels are reached, a pre-injection phase at 0.5 MPa is conducted to verify the airtightness of the injection system. The water pressure is then released before initiating the main injection. To ensure accurate data acquisition, all systems, including fluid injection pressure, loading stress, and AE signal recording, are synchronized within the same time domain by a master computer as a timing equipment. The measurement setup is detailed in Table 3. Following extensive preliminary trials, an injection rate of 100 mL/min was selected to induce fracturing within a reasonable duration. This rate ensures the generation of sufficient acoustic emission signals and clear fracture phenomena for analysis.

3. Results and discussion based on AE event localisation

3.1. Evolution of AE events in cubic coal sample

The waveforms recorded during injection are processed using the simplex method to map the evolution of AE events. The simplex method, a global optimization algorithm first proposed by Dantzig [12], has been further refined by Ge [25,26]. In its modified form, this method identifies the first activated sensor as the centroid of an iteratively updated tetrahedroid, with a diameter ranging from one-third to one-half of the sensor array's length. In this experiment, since the AE sensors are positioned along the surrounding walls of the sample, the AE events are expected to originate within the sample itself. To enhance computational efficiency, the centroid of the iterated tetrahedroid, defined as having a diameter equal to half of the sample's length, is initially set at the centre of the cubic sample. The relationship between time and distance is expressed as follows:

$$\sqrt{(x_i - x_0) + (y_i - y_0) + (z_i - z_0)} = v_i(t_i - t_0) \tag{1}$$

where (x_i, y_i, z_i) is coordinates of sensors; (x_0, y_0, z_0) is coordinates of AE events; v_i and t_i are traveling velocities and times from the source to sensors; and t_0 is the occurrence time of AE event. Every iteration can generate a new set of (x_0', y_0', z_0'), t_{trav}' and t_0' which will be subtracted by the original recorded time to estimate time errors are used to be compared with the error threshold. As shown in the subset of Fig. 2, our vertices of first tetrahedroid are denoted as (A, B, C, D), each of which is used as a hypocenter to get a time error.

$$e = t_i - t_{trav} - t_0' \tag{2}$$

Fig. 2 provides a workflow chart for realization of simplex optimization method. Assuming that the vertex A has the biggest error e_a, and

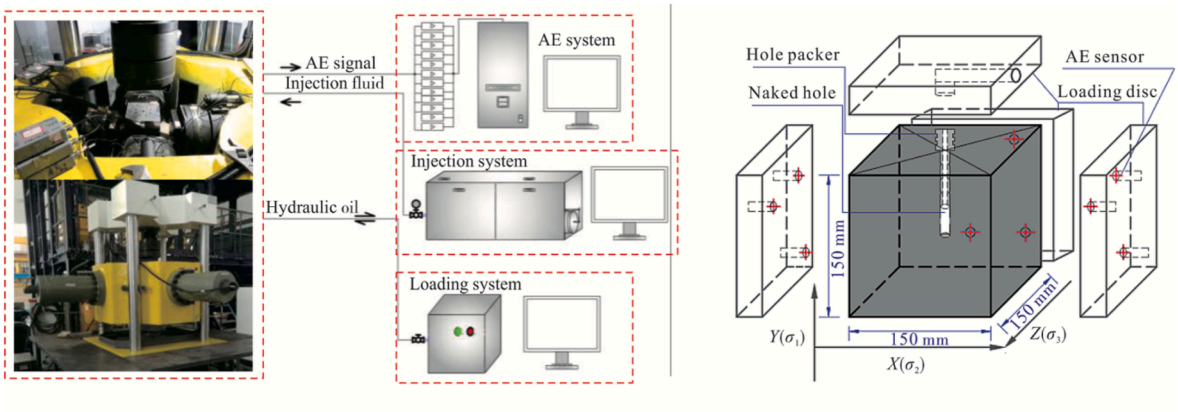

(a) Schematic of truly triaxial HF system

(b) Sample configuration (the origin of coordinate system is at the bottom corner of the cubic)

Fig. 1. Loading and monitoring equipment for coal sample hydraulic fracturing.

Table 2
Coordinates of AE sensors (sensor name: R15α).

Sensor	S01	S02	S03	S04	S05	S06	S07	S08	S09	S10	S11	S12
X (mm)	150	150	150	120	100	50	0	0	0	30	120	100
Y (mm)	100	120	50	30	100	50	120	120	50	30	120	50
Z (mm)	100	30	50	0	0	0	120	120	100	150	150	150

Table 3
Measurement set-up of hydraulic fracturing on coal sample.

Name	Value	Name	Value
AE monitoring		Injection	
AE recording threshold (dB)	38	σ_1, σ_2, σ_3 (MPa)	(2, 4, 6)
Sampling rate (kSPS)	500	Injection rate (mL/min)	100
Sensor operating frequency range (kHz)	50–200	Viscosity of injection water (Pa·s)	10^{-3}
Amplification (dB)	40	Data acquisition rate (Hz)	100

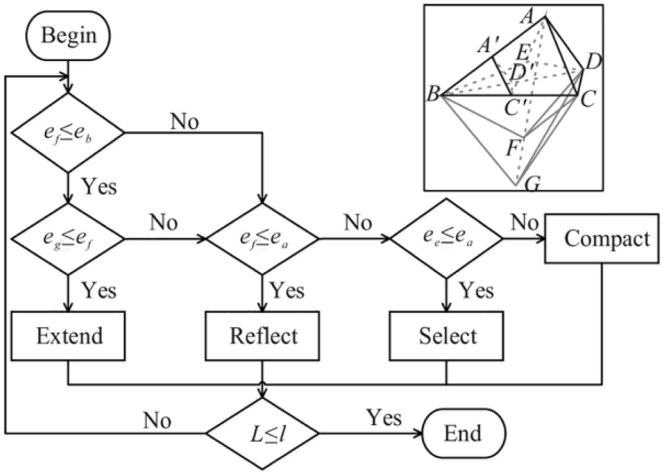

Fig. 2. Flow chart of simplex optimization method.

vertex B has the smallest error e_b, five steps can be conducted as follows to find a satisfying AE event:

(1) e_f is the time error of F that is symmetry point of A. If $e_f \leq e_b$, and then if $e_g \leq e_f$, where e_g is the time error of G that is the equally extending end of A, and then substitute A with G to construct a new tetrahedroid. This step is called *Extend*.

(2) If $e_g > e_f$, then $e_f \leq e_a$, substitute A with F to build a new tetrahedroid. This step is called *Reflect*.

(3) If $e_f > e_b$ and $e_f > e_a$, then compare the time error of centroid (E) of tetrahedroid (A, B, C, D) with e_a. If $e_e \leq e_a$, substitute A with E to get a new tetrahedroid. This step is called *Pick*.

(4) If $e_f > e_b$, $e_f > e_a$ and $e_e > e_a$, use B as the centroid and shorten other sides to half of what they are to build new tetrahedroid (B, H, I, J). This step is called *Compact*.

(5) Different tetrahedroids are iteratively updated from steps 1 to 4. In addition to accounting for time errors in this experiment, the perimeter of each tetrahedroid is calculated and compared against a predefined threshold to enhance spatial constraints on AE event points and accelerate convergence. If the new perimeter satisfies the set limit, the vertex with the smallest error is selected as the hypocenter. Otherwise, steps 1 to 4 are repeated until the limit is met.

The final tetrahedroid used for localisation has a calculated perimeter of 0.0329 m, remaining within the threshold of 0.04 m. The average side length of the tetrahedroid is approximately 5.5 mm which is much smaller than the diameter of injection borehole, accounting for less than 5 % of the 150 mm sample size, which will satisfy the accuracy identified by previous research [2]. The lowest recorded travel time error is 8.0514×10^{-6}.

A total of 539 AE events were recorded over a duration of 1200 s, as shown in Fig. 3. At 867 s, the coal sample fractured, leading to water leakage and an increase in the injection rate to 150 mL/min to ensure full fracture development. Under the higher injection rate, more pressure peaks were recorded, indicating intensified fracture propagation. Throughout the entire process, water pressure exhibited significant fluctuations. It remained at a low level until approximately 400 s, after which it increased rapidly. Notably, two distinct periods of peak water pressure were observed: between 700-800 s and 961–1100 s. However, AE energy did not follow a fluctuating trend. Instead, it exhibited a catastrophic spike near the peak of injection pressure. This AE energy

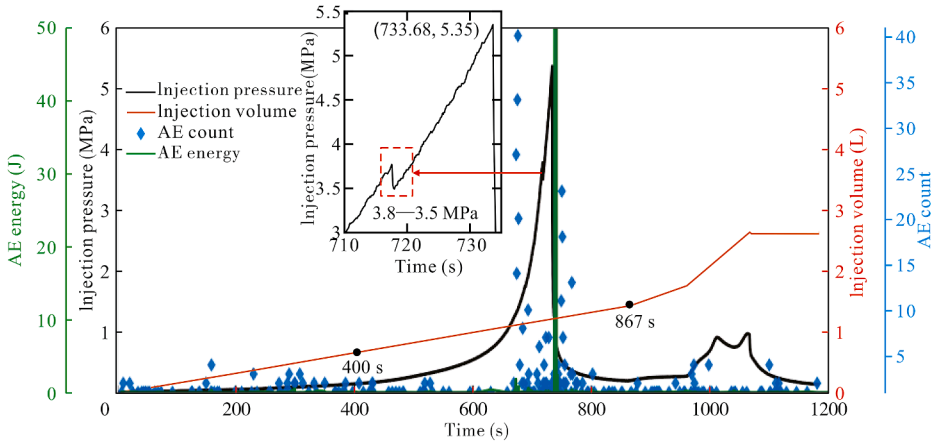

Fig. 3. Plot of water injections and AE parameters in coal sample hydraulic fracturing.

peak signifies the occurrence of the most intense fracturing event within the sample, which coincided with the onset of water leakage (peak injection pressure). The event rate, defined as the number of AE events occurring per second, showed two distinct peaks before and after the water pressure peak, particularly at 676 s and 734 s. A large number of small fractures were generated when the water pressure changed suddenly rather than at the moment of peak injection pressure.

Furthermore, very few AE events occurred immediately before the event rate peak at 676 s, which is even lower than earlier periods before 500 s. This 150 s interval (676-526 s) is characterized by a fracture-silent phase despite a rapid increase in injection pressure. This period of low event rate, referred to as a "silence gap," can serve as a precursor for predicting the approaching water pressure peak and the imminent fracturing of the sample. During the increase in water pressure, if the event rate declines and remains low for an extended period (exceeding 100 s in this experiment) before suddenly peaking, it can be inferred that both water pressure and AE energy will soon reach their maximum values, leading to sample failure within tens of seconds. After the initial peak, water pressure continues to rise, reaching additional peaks after 900 s due to the influence of principal stress. However, these subsequent pressure peaks are significantly lower than the first one. Correspondingly, AE activity and event rate responses are also much weaker due to the severe degradation of the sample's integrity and strength following the primary fracturing event.

At the first event rate peak, the water pressure reaches 1.39 MPa, exceeding the tensile strength of the coal sample (0.64 MPa) when considering the difference with the applied principal stress. Despite this, the injection volume continues to increase steadily, causing a rapid rise in water pressure. This moment, marked by the event rate peak, is defined as the initiation phase of fracturing. According to Biot's poroelasticity theory [27], the pressure required for fracture initiation around the borehole increases with greater porosity and permeability. This correlation suggests that the coal sample exhibits relatively high permeability, as indicated by the elevated pressure needed to induce fracturing.

As shown in Fig. 3, an oscillation in water pressure is observed at 718 s, with a sudden drop of 0.3 MPa. Despite the steady continuation of injection, the low number of AE events and minimal AE energy release suggest that fluid infiltration causes pre-existing fractures to intersect at a higher water pressure of 3.8 MPa, which is close to the secondary principal stress of 4 MPa. At the maximum injection pressure, the full breakdown of the sample is triggered, as evidenced by the largest AE energy release. The time delay between the pressure peak and the AE energy peak results from the dilatancy effect, a phenomenon previously observed in hydraulic fracturing tests on rocks [28]. This effect occurs because the formation of microfractures before complete failure increases compressive stress within the sample due to the increase of the permeability around the injection borehole, delaying the ultimate failure until peak injection pressure is reached.

Based on the observed AE event rate and the progression of injection pressure, the 1200 s water injection process can be broadly divided into three stages, as highlighted by black dots on injection volume curve in Fig. 3. At Stage 1 (0–400 s), this initial phase is characterised by a gradual increase in injection pressure, with only a sparse distribution of AE events, indicating minimal fracture activity. At Stage 2 (400–867 s), the injection pressure rises rapidly, accompanied by a significant increase in the AE event rate, and this stage marks the active fracturing period, where microcracks form and propagate extensively. At Stage 3 (867–1200 s), following the peak at 867 s, the injection pressure begins to decline. The fracture network is already well-developed, and AE activity decreases, signifying the stabilization of the fractured coal sample.

Fig. 4 illustrates the real-time variations in water injection at each time interval. The energy of AE events is calculated by integrating the squared waveform amplitude over the event duration [2]. Based on this, the event count, the total AE energy, and the average AE energy are computed for every 100 s, as shown in Fig. 4. Before the sample fractures, these three parameters exhibit fluctuations rather than a steady increase, indicating that the energy required for crack propagation is transferred non-uniformly throughout the sample. After the sample breaks, despite an increase in injection rate and a peak in the event count, both the total and average AE energy decline sharply, confirming that the sample has undergone physical rupture. Following the previously defined stages, the event locations for each stage are plotted in Figs. 5 and 6. Events occurring within the same stage are color-coded, and those with higher AE energy are highlighted with larger markers.

The centre of the sample lies the borehole, where the upper 60 mm (indicated by a thinner dashed line) represents the length of the hole packer, and the lower 30 mm (indicated by a thicker dashed line) is the naked borehole section used for hydraulic fracturing. During Stage 1, both the total AE energy and the event count remain low, with events sparsely distributed throughout the middle of the sample, lacking a clear dominant trend. In the *Z*-*Y* plane, AE events start propagating from the exposed borehole outward, forming a V-shaped distribution, with a greater concentration of events on the left side. In contrast, Stage 2 sees a significant increase in AE events, with the most intense events occurring in the upper part of the sample. Initially, during the first two periods (black and blue points), there is minimal expansion. Fig. 5 shows AE event distribution in different stages. Between 400 and 500 s, black points originate from the exposed borehole and extend outward in the positive *Z*-axis and *Y*-axis directions (Fig. 5f). The period from 528 to 669 s (blue points) represents a silent gap, where only a few events propagate along the previously established direction (black points).

Between 669 and 760 s in the *X*-*Z* and *Z*-*Y* planes (Fig. 5d and f), a large number of AE events extend radially outward from the borehole, clustering within the 50–140 mm range along the *Y*-axis. This period

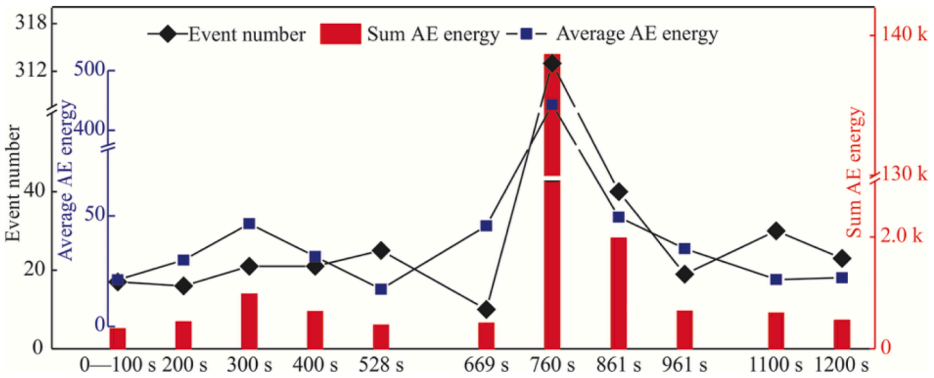

Fig. 4. Comparison of different AE parameters in different periods.

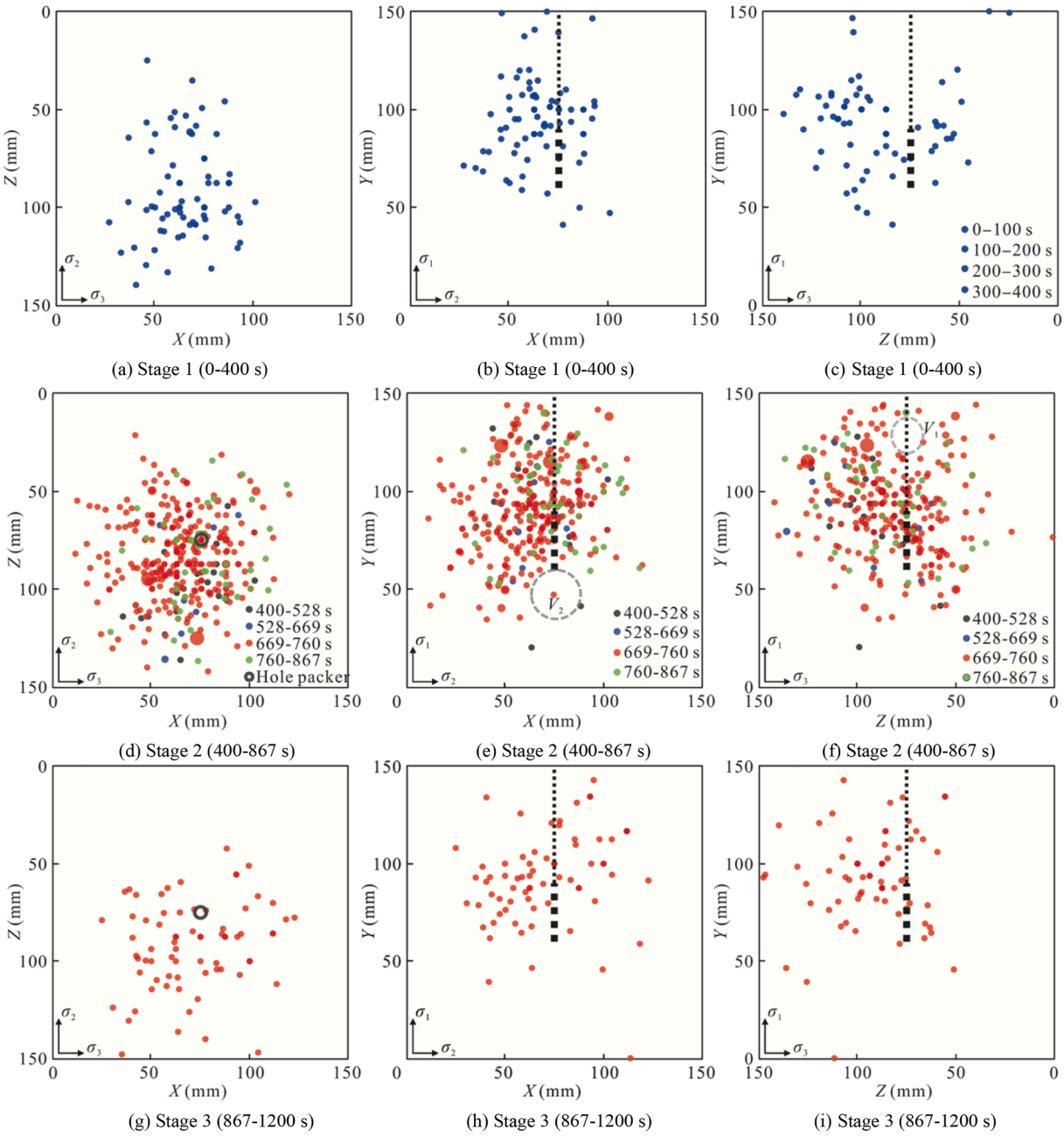

(a) Stage 1 (0-400 s) (b) Stage 1 (0-400 s) (c) Stage 1 (0-400 s)

(d) Stage 2 (400-867 s) (e) Stage 2 (400-867 s) (f) Stage 2 (400-867 s)

(g) Stage 3 (867-1200 s) (h) Stage 3 (867-1200 s) (i) Stage 3 (867-1200 s)

Fig. 5. AE event distribution in different stages.

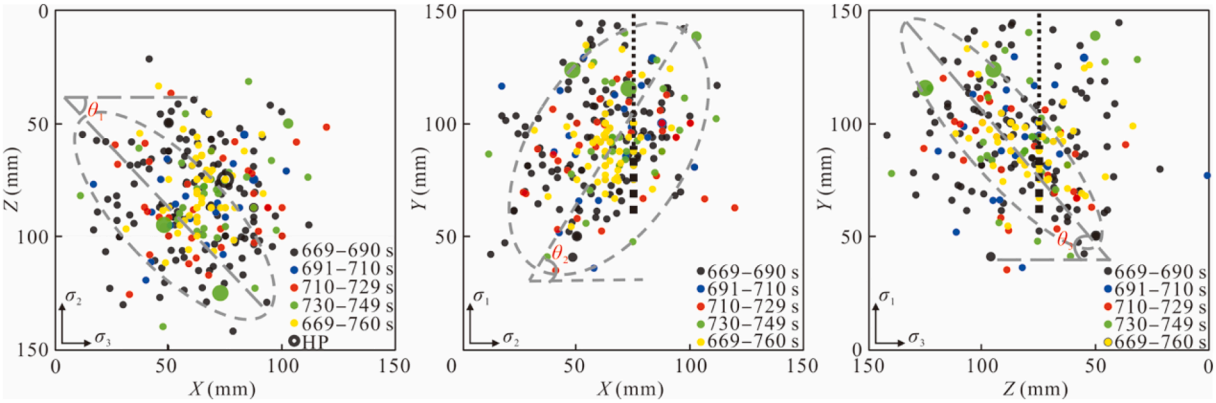

(a) Plane *X-Z* (b) Plane *X-Y* (c) Plane *Z-Y*

Fig. 6. AE events of 669–760 s.

outlines the overall fracture-affected region for the entire hydraulic fracturing process. Subsequently, green points indicate an upward propagation toward the positive *Z*- and *X*-axis directions in the *X-Z* plane and toward the positive *X*- and *Y*-axis directions in the *X-Y* plane (Fig. 5e), expanding towards the opposite side of the hole packer. Notably, Fig. 5e and 4f reveal a distinct absence of events at the top and bottom of the borehole, which refers to as fracture voids.

The upper fracture void (V_1) likely results from the strong adhesion of the hole packer to the sample and its distance from the exposed borehole section, reducing the likelihood of fracturing in this region. The lower fracture void (V_2) may stem from borehole drilling, which weakens the upper part of the sample more than the lower part. Consequently, the upper section fractures more easily under the combined influence of water pressure and principal stress. In Stage 3, most AE events remain within the previously defined fracture-affected area of Stage 2. The distribution in the *X-Y* plane (Fig. 5h) closely resembles that of Stage 2, while in the *X-Z* plane (Fig. 5g), most events are concentrated in the front half of the sample. Between 969 and 1062 s, additional AE events emerge, spreading farther outward. Since the sample was already fractured in Stage 2, water injection can no longer effectively transmit energy across the entire sample due to the formation of a major fracture plane. As a result, new fractures likely initiate and propagate laterally within the sample.

Since the points in stage 2 are densely clustered, they are further subdivided to better illustrate the sample's cracking development near the peak injection pressure during the 669–760 s interval. The data is divided into 20 s intervals, with the results shown in Fig. 6. Throughout the 669–760 s period, there are alternating patterns of contraction and expansion in the event distribution, although this feature is not present throughout the entire Stage 2. In the first 20 s interval (669–690 s, black points), the event rate peaks, causing many points to spread widely. In the next 20 s interval (691–710 s, blue points), the distribution shrinks considerably. In the *X-Z* plane (Fig. 6a), the blue points are distributed from the bottom left to the top right, while in the *Z-Y* plane (Fig. 6c), they extend from the bottom to the top. In the third interval (710–729 s, red points), the distribution extends further compared to the previous period, with points moving from the top left to the bottom right in the *Z-Y* plane and from the bottom left to the top right in the *X-Y* plane (Fig. 6b). During the fourth interval (730–749 s), the sample breaks as AE energy is rapidly released, causing the points to cluster near the borehole. Finally, in the last 12 s interval, the yellow points do not follow a continuous trend but instead form a zonal distribution around the exposed borehole, as the sample's fracture restricts energy transmission.

3.2. Quantitative interpretation of crack propagation

To interpret the alternative shrinks and expansions, the dynamic distribution in different periods is quantified in this section. First, the average distance from the injection borehole centre to all points in each period is calculated in each plan (*ZX*, *XY*, and *ZY*). Lines are drawn to connect the two points with the largest distance in each direction. For example, in the *Z* direction of the *X-Z* plane, a black line connects the two black points with the largest distance in a 20 s section. A similar line is drawn for the *X* direction in this plane. The lengths of these lines are then summed to be the *ZX* double length (shown in Fig. 7a). Based on the point distribution and period division in Figs. 5 and 6, the double lengths for the 669–760 s period are calculated and normalized, making it easier to present the results as curves in Fig. 7b. For comparison, the values in Stage 1 are calculated with 100 s intervals, due to the sparser distribution of AE events. The double length provides a representation of the overall area of event distribution in different periods, and the length ratio is also determined to compare point expansions in different directions.

For instance, the *Z/X* ratio is the double length line of *Z* direction divided by that of *X* direction in *Z-X* plan. All ratios are represented by curves in Fig. 7. Obviously, all these parameters have fluctuations with time. In Stage 1, the average distance and double length have alternative ups and downs. Events in *Z-X* plan are more concentrated in 100–200 s than 0–100 s and then go far away from the naked bore hole in the next 100 s and finally shrink again but still larger than the first period. For *Z-Y* plan, it has opposite changes than *Z-X* plan. The distance becomes larger in 100–200 s than 0–100 s and then waves up to 43 mm. Notably, the average distance has changes in three directions but never goes up or goes down at the same time. It indicates that when one direction extends away the other one or two would approach the bore hole. The mean value (the green curve called *XYZ* in Fig. 7) of average distances in three directions is taken as an indicator of events spatial distribution and it shows that the events have a volumetric expansion with water pressure increase.

Two curves represent the *ZX* and *ZY* double lengths, both normalized based on the value from the 0–100 s period. The red curve with circle symbols in Stage 1 stays below 1, indicating that the double length in the *Z-Y* plane decreases, resulting in a smaller area compared to the 0–100 s period. In contrast, the *Z-X* plane curve remains above 1, showing that the area continues to expand over time. The length ratio reflects the proportion of the largest distance in two directions within a plane. The *Z/Y* ratio remains near 1, except for an initial value of 1.39. This suggests that the *Z* and *Y* directions expand at a similar rate, while the *Z/X* ratio is consistently larger than 1, indicating that events in the *Z* direction propagate much faster than those in the *X* direction. The two curves also exhibit opposite trends, which highlights that, in addition to the average distance, the fracture area undergoes asynchronous expansions and contractions in different directions. In stage 1, the alternating shrinkages and expansions are evident, with the fracture space increasing over time and with rising water pressure. Notably, the

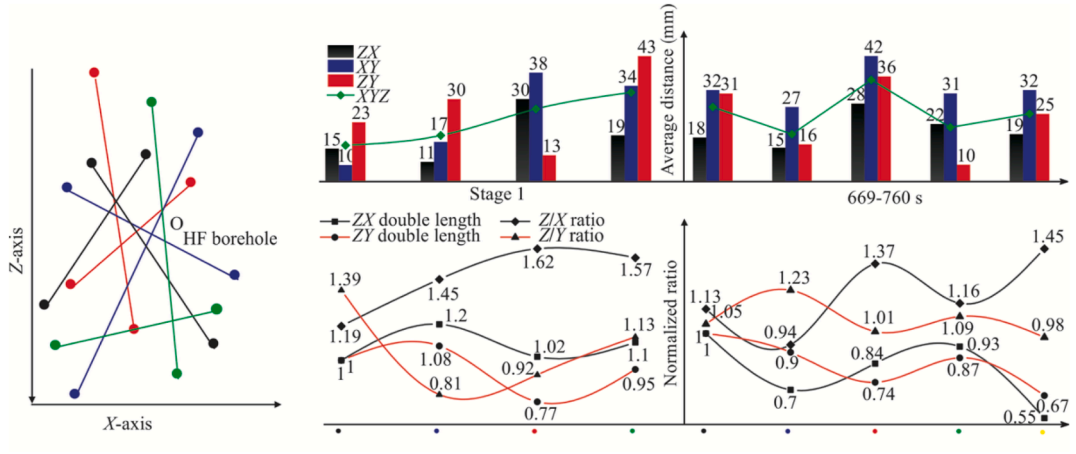

(a) Length sketch map

(b) Distribution parameters comparisons

Fig. 7. Comparison of AE events' extension.

expansion in the *Z* direction is more dominant.

The situation in 669–760 s is more complicated relatively. The average distance shows clear oscillations across all planes, with the mean value of the average distance (*XYZ* green curve) being larger than in Stage 1. Events in this time range run further away from the bottom of bore hole. The double length waves down and the events distribution finally shrinks to a small area. In the third period (709–729 s), the average distances in all three directions are significantly larger compared to other periods, yet their double lengths become relatively smaller. Additionally, both the *Z/X* and *Z/Y* ratios are greater than 1, with the *XY* average distance being the largest among all planes. These observations suggest that while the event distribution area is small, the locations of the events are farther from the exposed borehole section, further supporting the ongoing propagation of fractures in the *XY* plane. In the 729–749 s period, the average distances in all three directions indicate that the area is closer to the exposed borehole than in the earlier period, yet the expansion continues, as seen in the *ZX* and *ZY* double lengths. Furthermore, the *Z/X* and *Z/Y* ratios are around 1 (1.16 and 1.09), indicating that events are spreading equally in all directions at this moment, corresponding to the peak water pressure. Based on these three parameters, the intersection and breakdown phases are clearly distinguishable from each other.

After breakage, the smaller double length indicates that the event distribution shrinks sharply but extends farther than before. Combined with the length ratio, the final distribution forms a long and narrow area along the *Z* direction, as seen in Fig. 6. The overall volumetric distance (*XYZ*) in the 669–760 s period is higher than in Stage 1, although the maximum value is similar (32 mm vs. 35 mm). This may suggest that 35 mm is the maximum distance for event distribution in this 150 mm cubic coal sample. Fig. 7 also reveals an important observation about the average distances ($XY > ZY > ZX$): the *Y* direction is the dominant path for fractures. This contrasts with the *Z/Y* and *Z/X* length ratios, calculated from the double lengths. The double length represents an area, which can be strongly influenced by extreme event locations, whereas the average distance is a more statistical parameter that considers all events. This discrepancy implies that during the high-water-pressure period, most events tend to extend further along the *Y* direction, while extreme-distance events are more likely to occur along the *Z* direction. In contrast, during Stage 1, there is no such conflict, as the *Z* direction is nearly dominant in both the average distance and double length. The reasonable interpretation is that the principal stresses have more constrains to the geometry of hydraulic fractures when the injection energy stored is small. However, when the pore pressure has a high level of energy at peak value, the manipulation of principal stress will be weakened heavily.

3.3. Fracture geometry and the crack volume analysis

Based on the spatial distribution of events, the overall volume of the fractured space is calculated using the Convex Hull method [29]. Spatial envelope points are selected from all event points and connected by lines. The inner cubic space formed by all the connected envelope points is referred to as the fractured volume, as shown in the left image of Fig. 8. The fractured space produced during the 669–760 s period is marked in dark blue, while the space produced throughout the entire injection process is marked in light blue. The outline of the fractured space forms a sphere, consistent with the planes shown in Fig. 6. Compared to the entire fractured space, the AE events during breakage primarily occur in the upper part. The fractured volumes for all stages, as well as for the 669–760 s period, are calculated and divided by the volume of the coal sample to determine the fractured volume ratios, as shown in Table 4. The global fractured volume ratio for all stages is 0.24, while the fractured volume ratio for the 669–760 s period is 0.23. This indicates that most of the fractured space is formed during this duration.

The fracture plane of the fractured coal sample is constructed from AE events in Fig. 8. The area of constructed fracture plane is 12814 mm^2 which is nearly half of the area of one side face of the sample (22500 mm^2). The curved surface is partly parallel to the maximum principal stress (*Y*) but not perpendicular to the minimum principal stress (*Z*). The curved plane shows that the fracture plane is redirected along the *X* axis to form an irregular plan. The angles, θ_1 (45°) and θ_3 (60°) correspond to the *Z/Y* length ratio (nearly 1) and *Z/X* length ratio (>1) respectively. The max fractured distance of *Z* with value of 120.3 mm which is biggest among three directions, is the *Z*-axis maximum distance between all events. The max fractured distances of *X* and *Y* are about 108 mm. The volumetric distance (35 mm) indicates that most events happen surrounding the HF borehole. The strong AE energy of events is the key for sample's breakage which is proved by the water leakage from the sample after AE energy peak. As discussed earlier, the initiation fluid pressure causes the events blossom and it has smaller value compared and much time difference with the breakdown. Most of the fracture area and volume is produced by initiation (1.39 MPa) and the breakage is caused by the breakdown water pressure (5.35 MPa) which is smaller than the maximum principal stress and uniaxial compression strength (5.99 MPa). Comparison among the fractured volume ratio, the final fracture plane, the max fractured distance and the volumetric distance indicates that (AE) events is unable to capture all the failure of the coal sample during hydraulic fracturing. There exists extensive proportion of aseismic failure behaviours [30]. More recording devices are expected to be employed to have a more comprehensive description of the coal failure under injection.

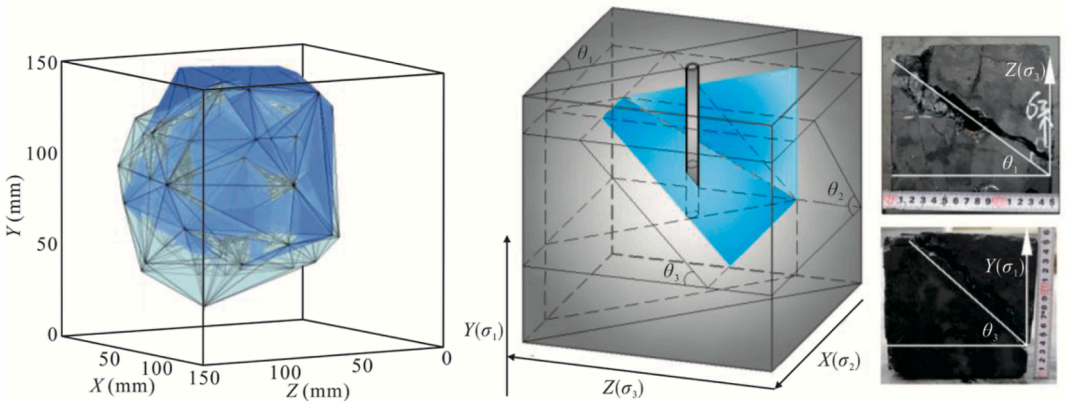

(a) Fracturing volume computed by AE events (b) Geometry of hydraulic fracture plane

Fig. 8. Quantification of hydraulic fractures in coal.

Table 4
Main parameters of coal sample hydraulic fracturing.

Principle stress (MPa)			Peak water pressure (MPa)	Initiation water pressure (MPa)	Max fractured distance (mm)			Volumetric distance (mm)	Fractured volume ratio	Fracture plane (mm^2)	Fracture orientation		
σ_1	σ_2	σ_3			X	Y	Z				θ_1	θ_2	θ_3
6	4	2	5.35	1.39	108.1	108.2	120.3	35	0.24/0.23	12814	45°	60°	50°

The fracture plane is not parallel to the direction of maximum principal stress (σ_1) or perpendicular to that of minimum principal stress (σ_3) as the theory deduces [31,32]. It assumes by theory that the sample being hydraulically fractured is uniform and homogeneous inside and the water pressure applies uniformly to borehole. Indeed, the coal is existing underground in a weak and cracked status. The sample with 150 mm has much possibility to contain preexisting fractures, which will dominate the path of pressurized fluid flow and lead to tortured fracture planes with unpredictable geometries [28]. As discussed in Section 3.1, the presence of preexisting fracture enhances the permeability of the coal, which makes the initiation injection pressure (1.39 MPa) larger than tensile strength (0.64 MPa) due to poroelastic effect. Moreover, the mechanical strength of the sample is determined by the mechanical test for standard cylinder samples. The size effect on tensile strength applies to the cubic sample, making it more easily to be cracked than cylinder samples. In practical application, greater fracture complexity will boost stress release to mitigate the probability of rock/coal burst and enhance the coal wettability, while demand more injection pressure and may also reduce the fracture extension distance. A thorough assessment of heterogeneity and anisotropy on large sample from target fracturing location needs to be developed with potential application of ultra sonic wave transmission. Injection design in terms of borehole spacing and injection times needs to be tailored by both assessment of heterogeneity and anisotropy and hydraulic fracturing experiments.

4. Conclusions

True triaxial hydraulic fracturing experiments were conducted using a self-developed apparatus with 150 mm cubic coal samples to optimise the injection strategy for rock/coal burst mitigation. Analysis of acoustic emission (AE) recordings and injection history revealed several key findings. The AE energy peak lags behind the water pressure peak due to the dilatancy effect, while the event rate reaches its maximum when water pressure experiences a sudden increase or drop. Most events occur between 50 and 120 mm along the direction of the maximum principal stress. During the sample's breakdown phase, alternating shrinkage and expansion (ASE) phenomena are observed. Parameters such as average event distance, double length, and length ratio effectively quantify the temporal distribution of fractures. Preexisting fractures introduce heterogeneity in the coal sample and play a dominant role in hydraulic fracture propagation. The fracture plane, reconstructed from AE events, forms an irregular surface that is partially aligned with the maximum principal stress, closely resembling the final fracture morphology of the cracked coal sample. The fracture plane occupies approximately half of one side of the coal sample, while the total fractured volume accounts for about one-fourth of the sample's total volume.

CRediT authorship contribution statement

Xin Zhang: Writing – original draft, Investigation, Formal analysis, Conceptualization. **Guangyao Si:** Writing – review & editing, Supervision, Funding acquisition, Conceptualization. **Anye Cao:** Writing – review & editing, Resources, Methodology, Data curation. **Changbin Wang:** Writing – review & editing, Visualization, Resources, Investigation. **Guozhen Zhao:** Writing – review & editing, Validation, Software, Formal analysis.

Declaration of competing interest

All authors declare that they have no known competing financial interests or personal relationships that could have appeared to influence the work reported in this paper.

Acknowledgments

Grant support from the Jiangsu Province International Collaboration Program-Key national industrial technology research and development cooperation projects in China (No.BZ2023050).

References

[1] R. Jeffrey, X. Zhang, Z. Chen, Hydraulic fracture growth in naturally fractured rock. Porous Rock Fracture Mechanics, Woodhead Publishing, 2017, pp. 93–116.

[2] X. Zhang, Seismic Characterisation of Rock Failure in Hydraulic Fracturing via Numerical Modelling and Laboratory Experiments, University of New South Wales, Australia, 2024.
[3] M.Y. Soliman, A. Rezaei, M. Khalaf, P. Gordon, C. Cipolla, Pulse power plasma stimulation: a technique for waterless fracturing, enhancing the near wellbore permeability, and increasing the EUR of unconventional reservoirs, Gas Sci. Eng. 122 (2024) 205201.
[4] J. Ramos, W.L. Wang, J. Diessl, N. Oliver, M.S. Bruno, Advanced hydraulic fracture characterization using pulse testing analysis, Rock Mech. Rock Eng. 52 (12) (2019) 5047–5069.
[5] H. He, L. Dou, J. Fan, T. Du, X. Sun, Deep-hole directional fracturing of thick hard roof for rockburst prevention, Tunn. Undergr. Space Technol. 32 (2012) 34–43.
[6] R. Jeffrey, K. Mills, X. Zhang, Experience and results from using hydraulic fracturing in coal mining, in: Proceedings of the 3rd International Workshop on Mine Hazards Prevention and Control, Brisbane, Australia, 2013, pp. 110–116.
[7] D. Song, Z. Liu, E. Wang, L. Qiu, Q. Gao, Z. Xu, Evaluation of coal seam hydraulic fracturing using the direct current method, Int. J. Rock Mech. Min. Sci. 78 (2015) 230–239.
[8] G. Ni, H. Xie, Z. Li, L. Zhuansun, Y. Niu, Improving the permeability of coal seam with pulsating hydraulic fracturing technique: a case study in Changping coal mine, China. Process, Saf. Environ. Prot. 117 (2018) 565–572.
[9] J.F. Hazzard, R.P. Young, Dynamic modelling of induced seismicity, Int. J. Rock Mech. Min. Sci. 41 (8) (2004) 1365–1376.
[10] X. Zhang, G. Si, Q. Bai, Z. Xiang, X. Li, J. Oh, Z. Zhang, Numerical simulation of hydraulic fracturing and associated seismicity in lab-scale coal samples: a new insight into the stress and aperture evolution, Comput. Geotech. 160 (2023) 105507.
[11] X. Zhang, G. Si, Q. Bai, B. Jiao, W. Cai, Effects of discrete fracture networks on simulating hydraulic fracturing, induced seismicity and trending transition of relative modulus in coal seams, Int. J. Coal Sci. Technol. 12 (1) (2025) 14.
[12] G.B. Dantzig, Application of the simplex method to a transportation problem, AAPA 13 (1951) 359–373.
[13] J. Bergstra, Y. Bengio, Random search for hyper-parameter optimization, JMLR 13 (1) (2012) 281–305.
[14] J.A. Vrugt, C.J.F. ter Braak, C.G.H. Diks, B.A. Robinson, Accelerating Markov Chain Monte Carlo simulation by differential evolution with self-adaptive randomized subspace sampling, IJNSNS 10 (3) (2009) 273–290.
[15] J. Qian, H. Zhang, E. Westman, New time-lapse seismic tomographic scheme based on double-difference tomography and its application in monitoring temporal velocity variations caused by underground coal mining, Geophys. J. Int. 215 (3) (2018) 2093–2104.
[16] Y. Zhang, W. Xie, DEPSO: hybrid particle swarm with differential evolution operator, Proc. IEEE Int. Conf. Syst. Man Cybern. 4 (2003) 3816–3821.
[17] N. Li, B. Huang, X. Zhang, Y. Tan, B. Li, Characteristics of microseismic waveforms induced by hydraulic fracturing in coal seam for coal rock dynamic disasters prevention, Saf. Sci. 115 (2019) 188–198.
[18] Y. Lu, L. Wang, Z. Ge, Z. Zhou, K. Deng, S. Zuo, Fracture and pore structure dynamic evolution of coals during hydraulic fracturing, Fuel 259 (2020) 116272.
[19] C. Lu, Z. Ge, Z. Zhou, Q. Li, J. Shangguan, S. Huang, Q. Deng, Experimental study on factors influencing interaction behaviors of hydraulic fractures and coal–rock interface: stress, interface and perforation, Rock Mech. Rock Eng. 58 (5) (2025) 5167–5183.
[20] H. Kang, Y. Xia, M. Feng, C. Lu, F. Gao, Case study of hydraulic fracturing for coal burst risk mitigation, Int. J. Coal Sci. Technol. 12 (1) (2025) 1–15.
[21] B.X. Huang, Y.Z. Wang, S.G. Cao, Cavability control by hydraulic fracturing for top coal caving in hard thick coal seams, Int. J. Rock Mech. Min. Sci. 74 (2015) 45–57.
[22] S. Stanchits, J. Burghardt, A. Surdi, Hydraulic fracturing of heterogeneous rock monitored by acoustic emission, Rock Mech. Rock Eng. 48 (6) (2015) 2513–2527.
[23] X. Shi, Y. Qin, Q. Gao, S. Liu, H. Xu, T. Yu, Experimental study on hydraulic fracture propagation in heterogeneous glutenite rock, Geo. Sci. Eng. 225 (2023) 211673.
[24] Z.T. Bieniawski, M.J. Bernede, Suggested methods for determining the uniaxial compressive strength and deformability of rock materials: part 1. Suggested method for determining deformability of rock materials in uniaxial compression, Int. J. Rock Mech. Min. Sci. Geomech. Abstr. 16 (2) (1979) 138–140.
[25] M. Ge, Comment on 'microearthquake location: a nonlinear approach that makes use of a simplex stepping procedure' by A, Prugger D. Gendzwill. BSSA. 85 (1) (1995) 375–377.
[26] M. Ge, Analysis of source location algorithms part II: iterative methods, J. Acoust. Emiss. 21 (1) (2003) 29–51.
[27] S. De Simone, C. Darcel, H.A. Diego Mas Ivars Kasani, Philippe Davy, Equivalent biot and skempton poroelastic coefficients for a fractured rock mass from a DFN approach, Rock Mech. Rock Eng. 56 (12) (2023) 8907–8925.
[28] X. Zhang, G. Si, J. Zhang, M. Wang, G. Zhao, J. Oh, Seismic characterisation of hydraulic fractures influenced by granitic coarse grains, Rock Mech. Rock Eng. 58 (2025) 6255–6275, https://doi.org/10.1007/s00603-025-04477-w.
[29] S. Missoum, P. Ramu, R.T. Haftka, A convex hull approach for the reliability-based design optimization of nonlinear transient dynamic problems, Comput. Methods Appl. Mech. Eng. 196 (29–30) (2007) 2895–2906.
[30] S.D. Goodfellow, M.H.B. Nasseri, S.C. Maxwell, R.P. Young, Hydraulic fracture energy budget: insights from the laboratory, Geophys. Res. Lett. 42 (9) (2015) 3179–3187.
[31] M.K. Hubbert, D.G. Willis, Mechanics of hydraulic fracturing, Petrol. Trans. AIME 210 (1) (1957) 153–168.
[32] X. Zhang, G. Si, J. Oh, G. Zhao, Evolution of crack source mechanisms in laboratory hydraulic fracturing on Harcourt granite, Rock Mech. Rock Eng. 57 (10) (2024) 7945–7961.